Published in final edited form as:
J Mol Biol. 2009 June 5; 389(2): 388–400. doi:10.1016/j.jmb.2009.04.022.

Structure and Mechanism of a Eukaryotic FMN Adenylyltransferase

Carlos Huerta[1], **Dominika Borek**[1], **Mischa Machius**[1], **Nick V. Grishin**[1,2], and **Hong Zhang**[1,*]

[1] Department of Biochemistry, University of Texas Southwestern Medical Center, Dallas, Texas 75390

[2] Howard Hughes Medical Institute, University of Texas Southwestern Medical Center, Dallas, Texas 75390

Abstract

Flavin mononucleotide adenylyltransferase (FMNAT) catalyzes the formation of the essential flavocoenzyme FAD and plays an important role in flavocoenzyme homeostasis regulation. By sequence comparison, bacterial and eukaryotic FMNAT enzymes belong to two different protein superfamilies and apparently utilize different set of active site residues to accomplish the same chemistry. Here we report the first structural characterization of a eukaryotic FMNAT from a pathogenic yeast *Candida glabrata* (*Cg*FMNAT). Four crystal structures of *Cg*FMNAT in different complexed forms were determined at 1.20–1.95 Å resolutions, capturing the enzyme active site states prior to and after catalysis. These structures reveal a novel flavin-binding mode and a unique enzyme-bound FAD conformation. Comparison of the bacterial and eukaryotic FMNATs provides a structural basis for understanding the convergent evolution of the same FMNAT activity from different protein ancestors. Structure-based investigation of the kinetic properties of FMNAT should offer insights into the regulatory mechanisms of FAD homeostasis by FMNAT in eukaryotic organisms.

Keywords

flavocoenzymes; FAD biosynthesis; adenylyltransferase; Rossmann-like fold; convergent evolution

INTRODUCTION

Flavin nucleotides FMN and FAD are essential cofactors involved in many redox reactions in the cell.[1] The chemical and functional versatility of these cofactors, in association with various flavoproteins, allows them to be involved in a large variety of different types of reactions and to participate in many cellular processes ranging from energy production, light emission, DNA repair, chromatin remodeling, and protein folding to detoxification, neural development, and apoptosis.[2; 3; 4] Riboflavin, also known as vitamin B2, is the universal precursor for the synthesis of FMN and FAD, the primary form of flavins in cells.[5; 6] Due to

*Corresponding authors: Hong Zhang, zhang@chop.swmed.edu, Phone: 214-645-6372, Fax: 214-645-5948.

the involvement of flavocofactors in wide-ranging metabolic processes, riboflavin deficiency leads to a multitude of physiological aberrations, such as abnormal fetal development, inadequate ion absorption, cardiovascular disease and corneal defects.[7]

In prokaryotes, yeast and plants, riboflavin is either synthesized *de novo*, or obtained from the environment and transported into the cells. [6,8] Higher eukaryotes, such as humans, lack the *de novo* riboflavin synthesis machinery and the only means of obtaining riboflavin is from the diet.[5; 6] The riboflavin transporter for eukaryotes has been identified in *Saccharomyces cerevisiae* and is encoded by gene *mch*5.[9] Converting riboflavin to FAD involves two universally conserved enzymes, riboflavin kinase (RFK) and flavin mononucleotide adenylyltransferase (FMNAT) (Fig. 1). Riboflavin kinase (ATP:riboflavin 5′-phosphotransferase, EC 2.7.1.26) phosphorylates riboflavin to generate flavin mononucleotide (FMN), while FMNAT (ATP:FMN adenylyltransferase, EC 2.7.7.2) adenylates FMN to form FAD. In bacteria, RFK and FMNAT are encoded in the same gene, *ribF* or *ribC*,[10; 11] and the protein product is referred to as FAD synthetase (FADS) with the FMNAT domain located at the N-terminus and the RFK domain at the C-terminus. In eukaryotes, RFK and FMNAT are encoded by separate genes.[12; 13] In higher eukaryotes, the gene encoding FMNAT also contains a second domain with sequence similarity to proteins involved in molybdenum-cofactor (MoCo) biosynthesis, such as MogA and MoeA.[14; 15] The potential function of this MoCo-binding protein-like domain is unknown.

Bacterial and eukaryotic RFKs are similar in sequence and structure, and they belong to a unique protein family containing only riboflavin kinases.[16; 17] In contrast, the evolutionary link between bacterial and eukaryotic FMNATs is less clear as they show little sequence similarity and are classified in different protein superfamilies in SCOP[18] or different clans in pfam[19] databases. The bacterial FMNAT domain of the bifunctional RFK/FMNAT belongs to the (H/T)xGH motif containing nucleotidylyl transferase superfamily, while eukaryotic FMNAT is currently classified as a member of the 3′-phosphoadenosine 5′-phosphosulfate (PAPS) reductase-like family belonging to the “adenine nucleotide α hydrolase-like” superfamily, which has conserved motifs different from those of nucleotidylyl transferases. Despite substantial differences in sequence and structure, the mammalian and bacterial FMNAT enzymes have similar kinetic properties.[20; 21] Both enzymes catalyze the formation of FAD through an ordered bi-bi mechanism and have the same substrate binding and product release order where ATP binds first to the enzyme followed by FMN, and product inorganic pyrophosphate (PP_i) is released first followed by the release of FAD. Pronounced product feedback inhibition was observed for rat liver FMNAT, and it was suggested that such a property would enable FMNAT to play a role in regulating cellular FAD homeostasis as the K_i values of FAD against FMN (0.75 μM) and Mg^{2+}ATP (1.3 μM) are close to the concentration of free FAD (0.4 μM).[21] Maintenance of FAD homeostasis is important, as several cellular processes, such as oxidative protein folding and homocysteine metabolism, are sensitive to FAD levels.[22; 23]

Both RFK and FMNAT are needed for generating the indispensable flavocofactors FMN and FAD.[6] The essentiality of the two enzymes has been established experimentally in bacterial[24] and yeast species,[12; 13; 22] and has been inferred to all other organisms. The significant differences between eukaryotic and bacterial FMNAT makes it a particularly attractive target for developing selective anti-infectious drugs.[24] Structural analysis of both eukaryotic and bacterial FMNATs will reveal the different configurations of the substrate binding and catalytic sites, which may benefit a structure-based inhibitor development effort. Such analysis will also address two fundamental questions: how eukaryotic and bacterial FMNAT accomplish the same chemistry with different active site architectures and what mechanistic controls are embedded in the enzyme to influence FAD homeostasis. Here we report the first structural characterization of a eukaryotic FMNAT from *Candida*

glabrata, an opportunistic yeast pathogen causing candidemia and invasive candidiasis.[25; 26] We have determined the crystal structures of *Candida glabrata* FMNAT (*Cg*FMNAT) in the apo-form and in three different complexed forms (with ATP, with substrate FMN and the ATP analog AMPCPP, and with products FAD and PP_i, respectively). These structures reveal a novel flavin-binding mode and the detailed catalytic site configuration that are likely shared among all eukaryotic FMNATs. Combined with the results from steady-state kinetic analysis, a mechanism for eukaryotic FMNAT catalyzed adenylyl transfer reaction is proposed.

RESULTS

Quality of the structures

The crystal structure of apo-*Cg*FMNAT was solved by the single-wavelength anomalous dispersion (SAD) phasing method using selenomethione as the source of anomalous dispersion and was refined against a native dataset to the resolution of 1.20 Å (Table 1). There is one *Cg*FMNAT molecule in the asymmetric unit. Crystal-packing analysis suggests that the functional unit of *Cg*FMNAT is a monomer, which is consistent with the gel filtration result that showed *Cg*FMNAT is monomeric in solution (see Fig. S1 available online). The refined model contains residues -3–304, except for residues 85–101, for which we found no associated electron density, and which are presumably disordered. Residues -3–0 (Gly-Ala-Met-Val) were introduced during cloning (see Supplementary Methods). The *Cg*FMNAT-ATP complex crystal is isomorphous to the apo-*Cg*FMNAT, and its model was refined to 1.87 Å resolution. This model contains residues -3–83, 103–304, and an ATP molecule with well defined density (Fig. 2a). Crystals of the substrate and product ternary complexes are isomorphous to each other and belong to the space group C2 with six monomers in the asymmetric unit. They were refined to resolutions of 1.95 Å and 1.35 Å, respectively. For the substrate ternary complex, the densities for AMPCPP and Mg^{2+} ion are well defined and double conformations of the AMPCPP phosphate tail are observed (Fig. 2b). The density for the phosphoribityl tail of FMN, on the other hand, is discontinuous, indicating significant conformational flexibility (Fig. 2b). For the product ternary complex, the densities for both products FAD and pyrophosphate (PP_i) are well defined (Fig. 2c). The flexible loop region (residues 84–100) disordered in the apo- and ATP-complexed *Cg*FMNAT structures is ordered in two of the six crystallographically independent *Cg*FMNAT monomers in the ternary complexes, presumably due to crystal-packing interactions. For all models, the main chain dihedral angles (φ, ψ) for each residue are in the allowed Ramachandran area. The exception is Gly224 in the ATP complex structure, which is associated with well defined electron density. Superposition of the C_α backbones of apo-protein, ATP complex and substrate ternary complex (monomer C) to product ternary complex (monomer B) gives a root mean square deviation (rmsd) of 0.42 Å, 0.41 Å, and 0.27 Å, respectively, indicating no substantial conformational changes among these structures (Fig. 2d).

Overall Structure

*Cg*FMNAT is composed of two domains (Fig. 3a). The N-terminal domain has an α/β fold with a central, twisted six-stranded β-sheet sandwiched by α-helices. The topology of this domain is a modified Rossmann-fold where the 5^{th} β-strand of the central β-sheet is anti-parallel to the rest of the strands (Fig. 3a). Comparison of *Cg*FMNAT with known protein structures using the Dali server[27] indicates that the core of *Cg*FMNAT is most similar to the members of the PAPS reductase-like protein family. These include bacterial adenosine 5′-phosphosulfate (APS) reductase[28] (PDB Id 2goy; Z-score of 15.4 and rmsd of 2.5 Å for 174 superimposed C_α atoms), PAPS reductase[29] (1sur, Z-score of 14.0 and rmsd of 2.4 Å for 159 superimposed C_α atoms), and ATP sulfurylase[30] (1zun, Z-score of 13.1 and rmsd of 2.9 Å

for 160 superimposed C_α atoms). Similar to *Cg*FMNAT, these protein also have an N-terminal domain of a modified Rossmann-fold topology (Fig. 3b). The C-terminal domain of *Cg*FMNAT is composed largely of loops (64%) interlaced by α6–α9 helices and two short 3_{10}-helices (Fig. 3a). This domain is much longer than that of APS and PAPS reductases and appears to be uniquely elaborated and expanded in yeast FMNAT (Supplementary Fig. S2). As will be discussed later, residues from this domain are also involved in interactions with ATP.

Mg^{2+}ATP Binding Site

The structures of the *Cg*FMNAT-ATP binary complex and the substrate ternary complex reveal details about the interactions between the enzyme and the ATP substrate. Five structural motifs are identified to be involved in ATP and Mg^{2+} binding (Fig. 3a). The *PP-loop motif*, extending from β1 to the N-terminus of α3, has the sequence of ^{60}SYNGGKDC$_{67}$ and is generally conserved in the superfamily. The *ADE motif*, named for ADEnine binding, corresponds to the LDTG motif in APS reductase[28] and consists of a short stretch of four residues, ^{107}FIDH$_{110}$, following strand β2. The first arginine-containing *ARG1 motif* (named Arg-loop in ref. [28]) is located in the loop connecting β4 to β5 and consists of residues ^{163}GIRHTD$_{168}$. The *γ-Phosphate motif* encompasses part of α7 and the following hairpin loop from the C-terminal domain situated above the nucleotide-binding site. Near the C-terminus of the protein, another arginine-rich motif, *ARG2*, of sequence ^{296}ERAGR$_{300}$ is also involved in nucleotide binding.

The ATP nucleotide binds in a crevice formed between β1 and β4, with its βγ-phosphate tail positioned in an anion-binding pocket near the N-terminus of α3 (Fig. 4a). A hydrogen-bond network is formed between ATP and residues from the five motifs (Fig. 4a). The adenine N1 nitrogen and N6 amino groups are hydrogen bonded to the main chain amide and carbonyl of Ile108 (part of the ADE motif), respectively. The N3 group of adenine forms a hydrogen bond to the side chain of Ser60 of the PP-loop motif, while the O2′ hydroxyl of ATP ribose interacts with the main chain carbonyl of Ser60. The O2′ hydroxyl forms another hydrogen bond with the main chain amide of Gly163 of the ARG1 motif. The PP-loop motif residues interacts extensively with the phosphates of ATP through both main chain and side chain moieties. The side chain of Asn62 interacts with the α-phosphate; the main chain amide of Cys67 interacts with the β-phosphate; and the side chain of Lys65 provides two hydrogen bonds to the γphosphate. Additional hydrogen-bonds to the γ-phosphate are formed with the Tyr216 hydroxyl and the Leu223 main chain amide. Both residues are from the γ-Phosphate motif (Fig. 4a).

In the presence of magnesium ions, as in the case of the substrate ternary complex structure, the AMPCPP phosphate tail adopts two distinct conformations (conformer I and II, Fig. 2b & Fig. 5) in different monomers of the six *Cg*FMNAT substrate ternary complexes in the asymmetric unit, both of which differ from that observed in the Mg^{2+}-free ATP binary complex structure (Fig. 5). The largest difference between these conformations is in the position of the β-phosphate, which moves 5.1 Å between conformer I and II, while the α- and γ-phosphates move 1.6 Å and 2.2 Å, respectively. In both conformers, the bound Mg^{2+} ion remains in the same position and maintains a six-ligand octahedral configuration (Fig. 5). In the first conformer, the Mg^{2+} is liganded to the β- and γ-phosphate oxygens, the Asp66 side chain carboxyl and three conserved water molecules, w2, w3, and w4 (Fig. 4a). W2 and w3 are further coordinated to the carboxylate group of Asp168 of the ARG1 motif. In the second conformer, all three AMPCPP phosphoryl moieties are coordinated to the Mg^{2+} ion, with the β-phosphate oxygen substituting the w4 water ligand. The β-phosphate in this conformation also interacts with Arg279 of the ARG2 motif through a bifurcated hydrogen bond (not shown). In the Mg^{2+}-free ATP binary complex structure, the position of the β-phosphate largely overlaps with the Mg^{2+} binding site (Fig. 5).

Compared to other PAPS reductase-like proteins, three of the five ATP binding motifs in *Cg*FMNAT, PP-loop, ADE and ARG1 motifs, are conserved (Fig. S2). Although the γ-Phosphate motif is also present in members of the PAPS reductase-like family such as APS reductase and bacterial ATP sulfurylase, its role in substrate binding and catalysis in these enzymes is not clear. Unique to *Cg*FMNAT and APS reductase is the presence of the ARG2 motif (Supplementary Fig. S2). In APS reductase, Arg242 and Arg245 near the protein C-terminus, corresponding to Arg297 and Arg300 of *Cg*FMNAT, provide important interactions with the phosphosulfate group of APS. Our preliminary kinetic analysis of the R297A mutant shows that the apparent $K_{m,ATP}$ and $K_{m,FMN}$ of the mutant increased ~5 and ~3 times, respectively, compared to the wild-type enzyme (data not shown), indicating that this Arg residue is indeed involved in substrate binding, presumably through interactions with the phosphoryl groups of the substrates.

FMN/FAD Binding Site

Unexpectedly, the flavin-binding site, as revealed in the substrate and product ternary complexes, is located on the same side of the central β-sheet as the adenosine moiety of ATP, where a deep trough is formed between the face of the β-sheet, helix α5, and the loop connecting the anti-parallel β5 to β6 (Fig. 3 & 4). This pocket forms a unique binding site for the flavin isoalloxazine ring that is different from those observed in any other FMN- or FAD-binding protein.[31] Residues from a broad range of structural elements are involved in the interaction with the isoalloxazine ring (Fig. 3a, & 4c). These include Met143 and Phe147 from helix α5, Ile160 to Ile162 from strand β4; Asp181, Trp184 and Phe187 from the loop connecting β5 to β6, and Arg189 from strand β6. These residues are highly conserved among eukaryotic FMNATs (Supplementary Fig. S3) and are collectively referred to as the *Flavin motif*. The isoalloxazine ring is sandwiched between the indole ring of Trp184 and the planar guanidinium group of Arg189. Deeply buried in the flavin-binding pocket is the hydrophobic dimethylbenzene moiety of the isoalloxazine ring, forming van der Waals contacts with hydrophobic side chains of Met143, Phe147, Ile160, Ile162, and Phe187 (Fig. 4b & 4c). The hydrophilic lumazine side of the ring forms two specific hydrogen bonds with the enzyme, between its C4 carbonyl and the main chain amide of Asp181, and between its N3 amide and the side chain of Asp 181, respectively. In both substrate and product ternary complex structures, the isoalloxazine group is also in van der Waals contact with the adenosine moiety of either AMPCPP or FAD, suggesting that the adenosine group is part of the isoalloxazine-binding pocket.

In contrast to the extensive interactions with the isoalloxazine ring, there are few contacts between the enzyme and the FMN phosphoribityl tail (Fig. 3b). As a result, the conformation of this part of the substrate is not well defined as indicated by the high B-factors, partial occupancy, and discontinuous density (Fig. 2b), In five of the six monomers in the asymmetric unit, FMN phosphoribityl tail is seen pointing toward the solvent, positioned over the N-terminus of helix α5 and away from the bound AMPCPP, probably due to electrostatic repulsion (Fig. 3b and 5). This observed conformation of FMN is apparently not in the catalytically ready state, as the phosphate is too far from the bound AMPCPP. Clearly the flexibility of FMN phosphoribityl tail would allow it to adopt multiple conformations and to move close to ATP so that the adenylyltransferase reaction could occur. Comparing the substrate and product ternary complexes, the positions of the isoalloxazine ring and the adenosine moieties remain essentially unchanged (Fig. 5). The phosphoribityl group of the product FAD becomes well ordered when covalently linked to the adenylyl group of ATP. The position of the PP_i product is also well defined in the crystal structure and is identical to that of the βγ-phosphates of AMPCPP in conformer I. The Mg^{2+} ion in the product ternary complex is coordinated to the PP_i, the adenylyl phosphate of FAD, Asp66 and two water molecules in a configuration with features of both AMPCPP

conformers in the substrate ternary complex (Fig. 5). Arg297 from the C-terminal ARG2 motif is found to interact with the diphosphate moiety of FAD (Fig. 3c), supporting its potential involvement in binding the phosphate groups of both ATP and FMN substrates, and positioning them for the adenylyl transfer reaction.

Steady-state kinetic properties of CgFMNAT

The steady-state kinetic parameters of *Cg*FMNAT were determined using a continuous coupled assay. The Lineweaver-Burk reciprocal plots of 1/*v* vs. 1/[FMN] and 1/*v* vs. 1/[ATP] (Fig. 6a and b) are consistent with an ordered bi-bi system,[32] with the substrate binding order being ATP first, followed by FMN. The same mechanism and substrate binding order were also proposed for rat liver and bacterial FMNATs in early studies.[20; 21] The initial rates of the reaction were globally fitted to the general equation for an ordered steady-state bireactant model (inserts of Fig. 6a and b). The steady-state kinetic parameters obtained for *Cg*FMNAT are: K_m for ATP 10.7 ± 2.3 μM, K_m for FMN 0.76 ± 0.15 μM, and k_{cat} 0.087 s^{-1}. The $K_{m,\ FMN}$ value for *Cg*FMNAT is similar to that obtained for human FMNAT isoform II in a recent study (apparent $K_{m,\ FMN}$ 0.36 ± 0.06 μM), while the k_{cat} appears to be more than ten times higher than that of the human enzyme (0.0036 ± 0.0001 s^{-1}).[33] These values are somewhat different from those obtained for the endogenous rat-liver FMNAT, where the apparent K_m for ATP and FMN are 71 μM and 9.1 μM, respectively, and V_{max} is 345 nmol FAD/min/mg protein, corresponding to a k_{cat} of 0.15 s^{-1}.[21]

Proposed mechanism for CgFMNAT

The four high-resolution structures of *Cg*FMNAT (apo form, complexes with ATP, with substrate FMN+AMPCPP, and with products FAD+PP_i) along with the kinetic data allow us to envision the events in the enzyme active site during catalysis (Fig. 6c and Supplementary Movie). In this process, ATP binds preferably first to the enzyme, because its binding pocket would be partially blocked by FMN, which binds at a site closer to the surface (Fig. 7). Additionally, binding ATP first may help to properly position the FMN substrate as the C8M methyl group of the isoalloxazine ring is packed against the adenosine moiety of the bound ATP. These observations are consistent with the substrate-binding order deduced from the kinetic data. The binding of ATP induces small adjustment (0.3–0.5 Å) of several surrounding residues, including Asn62, Lys65, Asp66, Ile108, and Asp168, presumably to optimize their interactions with Mg^{2+} and ATP. In the presence of Mg^{2+}, the phosphate tail of ATP can adopt either of the two discrete conformations I or II, in which the Mg^{2+} ion position remains the same (Fig. 5). Upon subsequent binding of FMN, side chains of several residues around the isoalloxazine ring, e.g., Met143, Phe147, Asp181 and Trp184, also make small adjustments to optimally interact with the substrate. Due to the lack of interaction between the enzyme and the phosphoribityl tail of FMN, this part of the FMN substrate is highly flexible and able to adopt multiple conformations. For the adenylation reaction to occur, the FMN phosphate would move close to the α-phosphate of ATP for the ensuing nucleophilic attack. The presence of Mg^{2+} ion and interaction with Arg297 (and potentially Arg300) of the ARG2 motif may help to overcome the electrostatic repulsion between the phosphate groups of the two substrates, and position FMN phosphate for the attack on the α-phosphate of ATP (Fig. 6c). The cleavage of the αβ-phosphodiester bond is facilitated by the coordination of the Mg^{2+} ion, which is required for the reaction. The Mg^{2+}ATP in the Conformer I position appears to be the catalytically competent conformation which allows the FMN phosphate group to approach the α-phosphate from the direction opposite the β-phosphate for the direct in-line nucleophilic attack. Minimal structural rearrangements are observed after product formation. The leaving diphosphate group is practically in the same position as the βγ-phosphates of the Conformer I of the nucleotide and interacts with the same set of protein residues and Mg^{2+} ion. The transferred

α-phosphate moves about 2.5 Å away from its original position and is now directly liganded to the Mg^{2+} ion (Fig. 5 and see Supplementary Movie). Earlier kinetic studies of rat liver FMNAT revealed that the enzyme is markedly inhibited by the product FAD with a K_i against FMN of 0.75 μM and a K_i against Mg^{2+}ATP of 1.3 μM.[21] It has been suggested that the biosynthesis of FAD is most likely regulated by product FAD at the last FMNAT step of the pathway.[21] Although not yet determined explicitly, our observation that *Cg*FMNAT copurifies with intrinsically bound FAD, along with the extensive interactions between the enzyme and FAD seen in the crystal structure, suggests that FAD binds to *Cg*FMNAT with high affinity and likely exerts a feedback inhibitory effect as well.

DISCUSSION

Our high-resolution structures of yeast FMNAT present the first characterization of a eukaryotic version of this essential enzyme. Although the overall structure of *Cg*FMNAT shares significant similarity with PAPS reductase-like family of proteins, as reflected in several shared nucleotide binding motifs. The mode of flavin binding in *Cg*FMNAT has not been observed before. In a 2001 survey by Dym and Eisenberg,[31] all FAD-binding proteins with known 3D structures were categorized into four different groups, represented by glutathione reductase, ferredoxin reductase, *p*-cresol methylhydroxylase and pyruvate oxidase, respectively. *Cg*FMNAT is clearly distinct from any of these FAD-binding proteins in both the conserved sequence motifs and flavin-binding mode. In other Rossmann-fold FAD-binding proteins (e.g., glutathione reductase and pyruvate oxidase groups) the isoalloxazine ring of FAD invariably binds on the side of the central β-sheet opposite from the adenine moiety and across the top of the sheet between β1 and β4. It often interacts with residues from another domain. In contrast, in *Cg*FMNAT, the isoalloxazine ring binds to the same side of the central β-sheet as the adenine, and the binding involves exclusively residues from the Rossmann-like N-terminal domain. The deviation from the typical Rossmann-fold topology, characterized by an anti-parallel strand β5 at the edge of the β-sheet, opens up the side of the β-sheet to form the flavin-binding pocket. In the *Cg*FMNAT product ternary complex structure, FAD adopts a bent conformation with adenosine moiety and isoalloxazine ring pack against each other. While the FAD cofactor in most flavoproteins adopts an extended conformation, bent FAD has been observed in flavodoxin reductase and DNA photolyase.[31] Yet, the conformations of these bent FADs are very different from that in *Cg*FMNAT (Fig. 8), emphasizing further the unique flavin-binding mode of eukaryotic FMNAT.

A comparison of the structures of *Cg*FMNAT, a prototypical eukaryotic FMNAT, and bacterial FMNAT as exemplified by *Tm*FADS[34] revealed remarkable differences in substrate binding modes and in the catalytic site configurations. *Tm*FADS belongs to the large nucleotidylyl transferase superfamily with the signature (H/T)xGH motif located between the end of the first β-strand and the first helix of the Rossmann-fold core. It has a different conformation from that of the corresponding PP-loop region of *Cg*FMNAT (Fig. 9). The second conserved motif of the nucleotidylyl transferase superfamily, ISSTxxR, is located at the N-terminal end of an α-helix in a C-terminal subdomain and interacts with the β- and γ-phosphates of the ATP nucleotide. No equivalent structural motif corresponding to ISSTxxR motif exists in *Cg*FMNAT, though the γ-Phosphate motif appears to perform a similar role. Most strikingly, the bound adenine nucleotides in the two proteins are orientated in opposite directions with regard to the plane of the central β-sheet (Fig. 9), delineating two completely different nucleotide-binding modes in these two protein superfamilies. Currently, no flavin-bound bacterial FMNAT structure is available. Based on the structural similarity of *Tm*FADS to other members of nucleotidylyl transferases, such as nicotinamide mononucleotide adenylyltransferases (NMNAT) for which extensive structural information are available,[35; 36; 37] the FMN substrate likely binds to a site corresponding to

the NMN-binding site in NMNAT on the opposite side of the central β-sheet from ATP so that the product FAD adopts a largely extended conformation (Fig. 9, right). Again, this arrangement is very different from the flavin-binding mode observed in *Cg*FMNAT (Fig. 9, left). Thus, eukaryotic and bacterial FMNAT present a remarkable case of ancient Rossmann-fold proteins that, after first diverging into two distinct protein families with different nucleotide-binding modes, have developed the same enzymatic activity via different active site configurations.

In summary, we present here high-resolution structures of a eukaryotic FMN adenylyltransferase in different complexed states, which revealed details about the active site configuration and a unique FAD-binding mode. The extensive interactions observed between the enzyme and the product FAD, and the lack of conformational changes after catalysis may explain why the enzyme is likely inhibited by the product. These structures lay a foundation for future investigation of the functional roles of active-site residues and the mechanism by which FMNAT influences FAD homeostasis in cells.

MATERIALS AND METHODS

Protein Expression and Purification

The predicted gene encoding *Cg*FMNAT (gi|50291750) was amplified from *Candida glabrata* genomic DNA (strain NCYC, ATCC36909D) by PCR and cloned into the *Nco*I and *Sal*I restriction sites of the pHIS parallel vector.[38] The plasmid was transformed into *E. coli* BL21(DE3) (Novagen), and the His_6-*Cg*FMNAT protein was expressed at 20 °C. His_6-*Cg*FMNAT was first loaded on a nickel-sepharose affinity column (GE Healthcare) equilibrated in Buffer A (20 mM HEPES, pH 8.0, 300 mM NaCl, 20 mM imidazole, 5% (v/v) glycerol and 1 mM DTT) and eluted with a gradient of 20–500 mM imidazole in Buffer A. The His_6-tag was cleaved by tobacco etch virus (TEV) protease during overnight dialysis at 4 °C and was removed from *Cg*FMNAT by passing through nickel-sepharose column a second time. As a second purification step, protein was loaded onto a Resource Q anion exchange column (GE Healthcare) equilibrated with Buffer B (20 mM HEPES, pH 7.5 and 5% (v/v) glycerol) and eluted with a 0–350 mM NaCl gradient, which yielded two pools. The first pool had a bright yellow color and was later shown to contain the *Cg*FMNAT-FAD complex. The second pool had a light yellow color, indicating the presence of flavin with partial occupancy. To remove the flavin and obtain homogeneous apo-*Cg*FMNAT, the second pool was incubated with 1.5 M $(NH_4)_2SO_4$ and purified by phenyl-sepharose hydrophobic-interaction chromatography (GE Healthcare). The final purification step for both *Cg*FMNAT-FAD and apo-*Cg*FMNAT consisted of a size exclusion chromatography column (Superdex 75 16/60, GE Healthcare) and the protein was eluted in 20 mM HEPES, pH 7.5, 150 mM NaCl, and 1 mM DTT. The selenomethionyl apo-*Cg*FMNAT was expressed in *E. coli* BL21(DE3) grown in minimal media supplemented with selenomethionine and other nutrients, and purified using the same procedure as for apo-*Cg*FMNAT.

Crystallization

All crystals were grown using hanging-drop vapor diffusion methods. For apo-*Cg*FMNAT and ATP complex crystallization, the reagents and greased 24-well plates were chilled on ice before setting up crystallization drops. The apo-*Cg*FMNAT crystals were grown by mixing 1.5 μl of protein (24 mg/ml in the gel filtration column buffer) with 1.5 μl of reservoir solution composed of 0.1 M Na acetate, pH 4.4–5.4 and 6–12% (w/v) PEG 4000, and equilibrating against the reservoir at 16°C. Prism-shaped apo-*Cg*FMNAT crystals grew to a maximum size of $0.55 \times 0.35 \times 0.35$ mm^3 within several days. Selenomethionyl apo-*Cg*FMNAT crystals were grown under similar conditions as the native protein. The

*Cg*FMNAT-ATP complex crystals were grown in the presence of 10 mM ATP under similar conditions as those for apo-*Cg*FMNAT. The co-crystals of *Cg*FMNAT substrate ternary complex were grown at 20 °C in the presence of 0.2 mM FMN and 5 mM AMPCPP under similar conditions as those for apo-*Cg*FMNAT, except that consecutive micro-seeding procedure was performed in order to obtain single crystals. The *Cg*FMNAT product ternary complex was obtained by adding 2 mM Na pyrophosphate to the *Cg*FMNAT-FAD pool (final protein concentration ~20 mg/ml in gel filtration buffer). The complex crystals were grown by mixing 1.5 μl *Cg*FMNAT-FAD-PP_i complex with 1.5 μl reservoir solution composed of 0.1 M Na acetate, pH 4.4–5.4, 0.2 M $MgSO_4$ and 20–26% (w/v) PEG MME 2000, and equilibrating against the reservoir at 20°C. All crystals were cryoprotected in a solution containing all the reservoir components and increments of glucose (10%, 20% and 30%), flash-frozen in liquid propane and stored in liquid nitrogen. For cryoprotecting the substrate ternary complex crystals, 5 mM $MgSO_4$ was also added along with glucose.

Data collection, X-ray structure determination and refinement

The 2.18 Å single-wavelength anomalous diffraction (SAD) data from a selenomethionyl apo-*Cg*FMNAT crystal was collected at the absorption edge (K-edge) of selenium at beam-line 19-BM; the 1.20 Å native apo-*Cg*FMNAT and 1.35 Å *Cg*FMNAT product ternary complex data sets were collected at beam-line 19-ID at the Advance Photon Source (APS), Argonne National Laboratory. The 1.87 Å dataset for the ATP complex and the 1.95 Å dataset for the substrate ternary complex were collected in-house with X-ray from a rotating anode generator (Rigaku FRE SuperBright), recorded on an RAXIS IV++ (Rigaku) image plate detector. All data were processed with either the HKL2000 or the HKL3000 package.[39; 40] Data collection statistics are presented in Table 1. The initial phases for apo-*Cg*FMNAT were obtained by the SAD phasing method (see Supplementary Methods for details), while the phases of all complexes were determined by the molecular replacement method using program MolRep[41] and the refined apo-*Cg*FMNAT as the search model. The refinements were performed using REFMAC[42] or PHENIX,[43] and manual model building was performed with Coot.[44] Models were assessed by MolProbity.[45]

Steady-State Kinetics

Steady-state kinetic parameters were determined using a continuous coupled assay (EnzChek® pyrophosphate assay kit, Molecular Probes®) with modifications. The reaction mixture (0.5 ml) contained 20 mM HEPES, pH 7.5, 2 mM $MgCl_2$, 0.5 units purine nucleoside phosphorylase, 0.015 units inorganic pyrophosphatase, 0.2 mM MESG (2-amino-6-mercapto-7-methylpurine riboside), 21 nM (10.5 pmol or 378 ng) apo-*Cg*FMNAT, 2.5 to 20 μM FMN, and 1 to 250 μM ATP. All enzyme reactions were carried out in duplicates and performed at 25 °C. The reaction was initiated by the addition of ATP, and the progress was monitored at 360 nm for 5 minutes. Steady-state kinetic parameters were determined by fitting the initial rates to the general equation describing a bireactant ordered bi-bi system (1).[32]

$$v=\frac{V_{max}[ATP][FMN]}{(K_{iATP}K_{mFMN}+K_{mFMN}[ATP]+K_{mATP}[FMN]+[ATP][FMN])} \quad (1)$$

K_{mATP} and K_{mFMN} are the Michaelis-Menten constants, and K_{iATP} is the dissociation constant for an ATP-enzyme complex. A nonlinear least-squares method as implemented in the Sigma Plot Enzyme Kinetics module (Systat Software) was used to fit the data.

Accession codes

The coordinates and structures factors were deposited in the Protein Data Bank with accession codes 3FWK for apo-*Cg*FMNAT, 3G59 for *Cg*FMNAT·ATP complex, 3G5A for *Cg*FMNAT·FMN·AMPCPP·Mg^{2+} complex and 3G6K for *Cg*FMNAT·FAD·PP_i·Mg^{2+} complex.

Supplementary Material

Refer to Web version on PubMed Central for supplementary material.

Acknowledgments

We thank Zbyszek Otwinowski for help with synchrotron data collection and initial SAD phasing. This work is supported by a grant from Welch Foundation (I-5105). C.H. is supported by National Institutes of Health Training Grant T32 GM008297. Results shown in this report are derived from work performed at Argonne National Laboratory (ANL), Structural Biology Center at the Advanced Photon Source. ANL is operated by UChicago Argonne, LLC, for the U.S. Department of Energy, Office of Biological and Environmental Research under contract DE-AC02-06CH11357.

Abbreviations

FMNAT	flavin mononucleotide adenylyltransferase
RFK	riboflavin kinase
FADS	flavin adenine dinucleotide synthetase
NMNAT	nicotinamide mononucleotide adenylyltransferase
AMPCPP	α,β-methyleneadenosine 5′-triphosphate
PAPS	3′-phospho-adenosine 5′-phosphosulfate
APS	adenosine-5′-phosphosulfate
SAD	single anomalous dispersion

References

1. Massey V. The chemical and biological versatility of riboflavin. Biochem Soc Trans 2000;28:283–96. [PubMed: 10961912]
2. Müller, F., editor. Chemistry and Biochemistry of Flavoenzymes. Vol. I. CRC Press; Boca Raton, FL: 1991.
3. Joosten V, van Berkel WJ. Flavoenzymes. Curr Opin Chem Biol 2007;11:195–202. [PubMed: 17275397]
4. van Berkel, WJH. Wiley Encyclopedia of Chemical Biology. John Wiley & Sons, Inc; 2008 Aug 15. Chemistry of Flavoenzymes.
5. Merrill AH Jr, Lambeth JD, Edmondson DE, McCormick DB. Formation and mode of action of flavoproteins. Annu Rev Nutr 1981;1:281–317. [PubMed: 6764718]
6. Fischer M, Bacher A. Biosynthesis of flavocoenzymes. Nat Prod Rep 2005;22:324–50. [PubMed: 16010344]
7. Powers HJ. Riboflavin (vitamin B-2) and health. Am J Clin Nutr 2003;77:1352–60. [PubMed: 12791609]
8. Vogl C, Grill S, Schilling O, Stulke J, Mack M, Stolz J. Characterization of riboflavin (vitamin B2) transport proteins from Bacillus subtilis and Corynebacterium glutamicum. J Bacteriol 2007;189:7367–75. [PubMed: 17693491]
9. Reihl P, Stolz J. The monocarboxylate transporter homolog Mch5p catalyzes riboflavin (vitamin B2) uptake in Saccharomyces cerevisiae. J Biol Chem 2005;280:39809–17. [PubMed: 16204239]

10. Manstein DJ, Pai EF. Purification and characterization of FAD synthetase from *Brevibacterium ammoniagenes*. J Biol Chem 1986;261:16169–16173. [PubMed: 3023344]
11. Coquard D, Huecas M, Ott M, van Dijl JM, van Loon AP, Hohmann HP. Molecular cloning and characterisation of the ribC gene from Bacillus subtilis: a point mutation in ribC results in riboflavin overproduction. Mol Gen Genet 1997;254:81–4. [PubMed: 9108293]
12. Santos MA, Jimenez A, Revuelta JL. Molecular characterization of FMN1, the structural gene for the monofunctional flavokinase of *Saccharomyces cerevisiae*. J Biol Chem 2000;275:28618–28624. [PubMed: 10887197]
13. Wu M, Repetto B, Glerum DM, Tzagoloff A. Cloning and characterization of FAD1, the structural gene for flavin adenine dinucleotide synthetase of Saccharomyces cerevisiae. Mol Cell Biol 1995;15:264–71. [PubMed: 7799934]
14. Liu MT, Wuebbens MM, Rajagopalan KV, Schindelin H. Crystal structure of the gephyrin-related molybdenum cofactor biosynthesis protein MogA from Escherichia coli. J Biol Chem 2000;275:1814–22. [PubMed: 10636880]
15. Schrag JD, Huang W, Sivaraman J, Smith C, Plamondon J, Larocque R, Matte A, Cygler M. The crystal structure of Escherichia coli MoeA, a protein from the molybdopterin synthesis pathway. J Mol Biol 2001;310:419–31. [PubMed: 11428898]
16. Karthikeyan S, Zhou Q, Mseeh F, Grishin NV, Osterman AL, Zhang H. Crystal structure of human riboflavin kinase reveals a beta barrel fold and a novel active site arch. Structure 2003;11:265–73. [PubMed: 12623014]
17. Cheek S, Zhang H, Grishin NV. Sequence and structure classification of kinases. J Mol Biol 2002;320:855–881. [PubMed: 12095261]
18. Murzin AG, Brenner SE, Hubbard T, Chothia C. SCOP: a structural classification of proteins database for the investigation of sequences and structures. J Mol Biol 1995;247:536–540. [PubMed: 7723011]
19. Finn RD, Tate J, Mistry J, Coggill PC, Sammut SJ, Hotz HR, Ceric G, Forslund K, Eddy SR, Sonnhammer EL, Bateman A. The Pfam protein families database. Nucleic Acids Res 2008;36:D281–8. [PubMed: 18039703]
20. Efimov I, Kuusk V, Zhang X, McIntire WS. Proposed steady-state kinetic mechanism for Corynebacterium ammoniagenes FAD synthetase produced by Escherichia coli. Biochemistry 1998;37:9716–23. [PubMed: 9657684]
21. Yamada Y, Merrill AH Jr, McCormick DB. Probable reaction mechanisms of flavokinase and FAD synthetase from rat liver. Arch Biochem Biophys 1990;278:125–30. [PubMed: 2157358]
22. Tu BP, Weissman JS. The FAD- and O(2)-dependent reaction cycle of Ero1-mediated oxidative protein folding in the endoplasmic reticulum. Mol Cell 2002;10:983–94. [PubMed: 12453408]
23. Hustad S, Ueland PM, Vollset SE, Zhang Y, Bjorke-Monsen AL, Schneede J. Riboflavin as a determinant of plasma total homocysteine: effect modification by the methylenetetrahydrofolate reductase C677T polymorphism. Clin Chem 2000;46:1065–71. [PubMed: 10926884]
24. Gerdes SY, Scholle MD, D'Souza M, Bernal A, Baev MV, Farrell M, Kurnasov OV, Daugherty MD, Mseeh F, Polanuyer BM, Campbell JW, Anantha S, Shatalin KY, Chowdhury SA, Fonstein MY, Osterman AL. From genetic footprinting to antimicrobial drug targets: examples in cofactor biosynthetic pathways. J Bacteriol 2002;184:4555–4572. [PubMed: 12142426]
25. Ostrosky-Zeichner L, Rex JH, Pappas PG, Hamill RJ, Larsen RA, Horowitz HW, Powderly WG, Hyslop N, Kauffman CA, Cleary J, Mangino JE, Lee J. Antifungal susceptibility survey of 2,000 bloodstream Candida isolates in the United States. Antimicrob Agents Chemother 2003;47:3149–54. [PubMed: 14506023]
26. Krcmery V, Barnes AJ. Non-albicans Candida spp. causing fungaemia: pathogenicity and antifungal resistance. J Hosp Infect 2002;50:243–60. [PubMed: 12014897]
27. Holm L, Sander C. Dali: a network tool for protein structure comparison. Trends Biochem Sci 1995;20:478–480. [PubMed: 8578593]
28. Chartron J, Carroll KS, Shiau C, Gao H, Leary JA, Bertozzi CR, Stout CD. Substrate recognition, protein dynamics, and iron-sulfur cluster in Pseudomonas aeruginosa adenosine 5′-phosphosulfate reductase. J Mol Biol 2006;364:152–69. [PubMed: 17010373]

29. Savage H, Montoya G, Svensson C, Schwenn JD, Sinning I. Crystal structure of phosphoadenylyl sulphate (PAPS) reductase: a new family of adenine nucleotide alpha hydrolases. Structure 1997;5:895–906. [PubMed: 9261082]
30. Mougous JD, Lee DH, Hubbard SC, Schelle MW, Vocadlo DJ, Berger JM, Bertozzi CR. Molecular basis for G protein control of the prokaryotic ATP sulfurylase. Mol Cell 2006;21:109–22. [PubMed: 16387658]
31. Dym O, Eisenberg D. Sequence-structure analysis of FAD-containing proteins. Protein Sci 2001;10:1712–28. [PubMed: 11514662]
32. Segel, IH. Enzyme Kinetics: Behavior and Analysis of Rapid Equilibrium and Steady-State Enzyme Systems. Wiley-Interscience; New York: 1993.
33. Galluccio M, Brizio C, Torchetti EM, Ferranti P, Gianazza E, Indiveri C, Barile M. Over-expression in Escherichia coli, purification and characterization of isoform 2 of human FAD synthetase. Protein Expr Purif 2007;52:175–81. [PubMed: 17049878]
34. Wang W, Kim R, Yokota H, Kim SH. Crystal structure of flavin binding to FAD synthetase of Thermotoga maritima. Proteins 2005;58:246–8. [PubMed: 15468322]
35. Saridakis V, Christendat D, Kimber MS, Dharamsi A, Edwards AM, Pai EF. Insights into ligand binding and catalysis of a central step in NAD+ synthesis: structures of Methanobacterium thermoautotrophicum NMN adenylyltransferase complexes. J Biol Chem 2001;276:7225–32. [PubMed: 11063748]
36. Zhang H, Zhou T, Kurnasov O, Cheek S, Grishin NV, Osterman A. Crystal structures of E. coli nicotinate mononucleotide adenylyltransferase and its complex with deamido-NAD. Structure (Camb) 2002;10:69–79. [PubMed: 11796112]
37. Zhou T, Kurnasov O, Tomchick DR, Binns DD, Grishin NV, Marquez VE, Osterman AL, Zhang H. Structure of human nicotinamide/nicotinic acid mononucleotide adenylyltransferase. Basis for the dual substrate specificity and activation of the oncolytic agent tiazofurin. J Biol Chem 2002;277:13148–54. [PubMed: 11788603]
38. Sheffield P, Garrard S, Derewenda Z. Overcoming expression and purification problems of RhoGDI using a family of “parallel” expression vectors. Protein Expr Purif 1999;15:34–9. [PubMed: 10024467]
39. Otwinowski Z, Minor W. Processing of X-ray diffraction data collected in oscillation mode. Methods Enzymol 1997;276:307–326.
40. Minor W, Cymborowski M, Otwinowski Z, Chruszcz M. HKL-3000: the integration of data reduction and structure solution--from diffraction images to an initial model in minutes. Acta Crystallogr D Biol Crystallogr 2006;62:859–66. [PubMed: 16855301]
41. Teplyakov, AVaA. MOLREP: an Automated Program for Molecular Replacement. Journal of Applied Crystallography 1997;30:4.
42. Murshudov GN, Vagin AA, Dodson EJ. Refinement of macromolecular structures by the maximum-likelihood method. Acta Crystallogr D Biol Crystallogr 1997;53:240–55. [PubMed: 15299926]
43. Adams PD, Grosse-Kunstleve RW, Hung LW, Ioerger TR, McCoy AJ, Moriarty NW, Read RJ, Sacchettini JC, Sauter NK, Terwilliger TC. PHENIX: building new software for automated crystallographic structure determination. Acta Crystallogr D Biol Crystallogr 2002;58:1948–54. [PubMed: 12393927]
44. Emsley P, Cowtan K. Coot: model-building tools for molecular graphics. Acta Crystallogr D Biol Crystallogr 2004;60:2126–32. [PubMed: 15572765]
45. Lovell SC, Davis IW, Arendall WB 3rd, de Bakker PI, Word JM, Prisant MG, Richardson JS, Richardson DC. Structure validation by Calpha geometry: phi, psi and Cbeta deviation. Proteins 2003;50:437–50. [PubMed: 12557186]
46. Merritt EA. Expanding the model: anisotropic displacement parameters in protein structure refinement. Acta Crystallogr D Biol Crystallogr 1999;55:1109–17. [PubMed: 10329772]
47. Potterton E, Briggs P, Turkenburg M, Dodson E. A graphical user interface to the CCP4 program suite. Acta Crystallogr D Biol Crystallogr 2003;59:1131–7. [PubMed: 12832755]
48. Ingelman M, Bianchi V, Eklund H. The three-dimensional structure of flavodoxin reductase from Escherichia coli at 1.7 A resolution. J Mol Biol 1997;268:147–57. [PubMed: 9149148]

49. Park HW, Kim ST, Sancar A, Deisenhofer J. Crystal structure of DNA photolyase from Escherichia coli. Science 1995;268:1866–72. [PubMed: 7604260]

50. Karplus PA, Schulz GE. Refined structure of glutathione reductase at 1.54 A resolution. J Mol Biol 1987;195:701–29. [PubMed: 3656429]

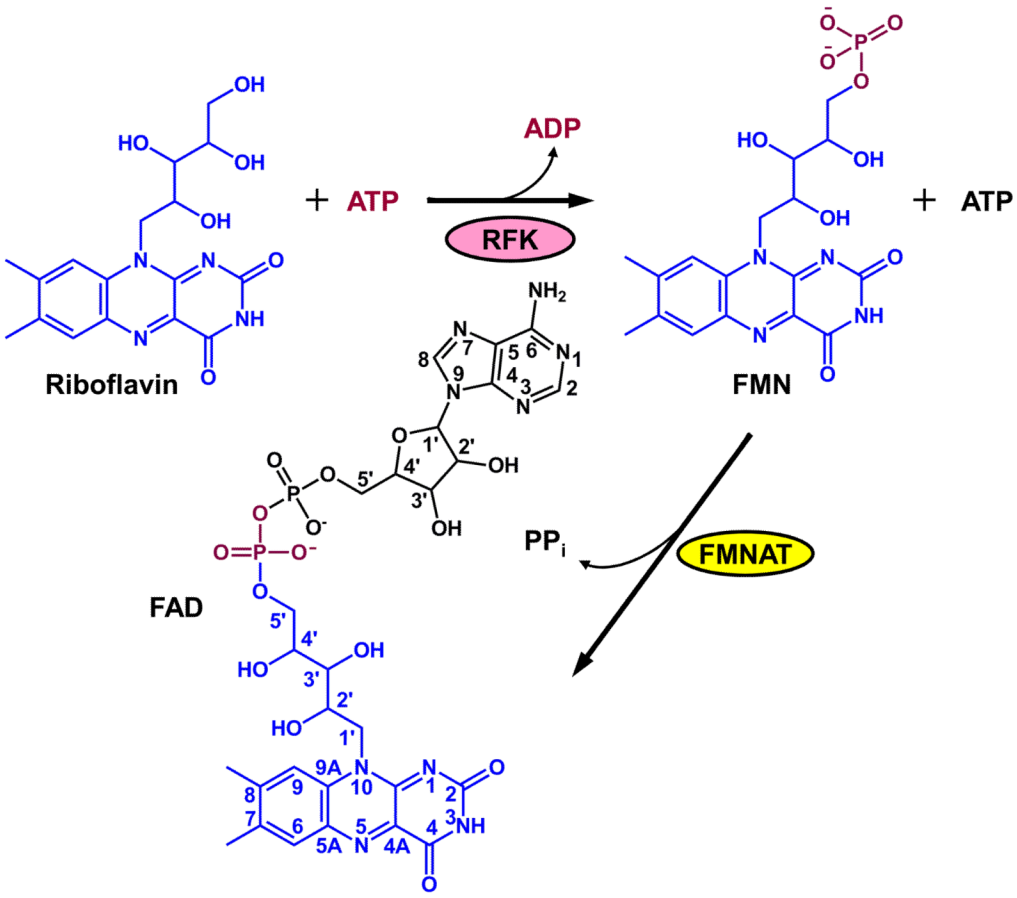

Figure 1.
Reactions catalyzed by riboflavin kinase (RFK) and FMN adenylyltransferase (FMNAT).

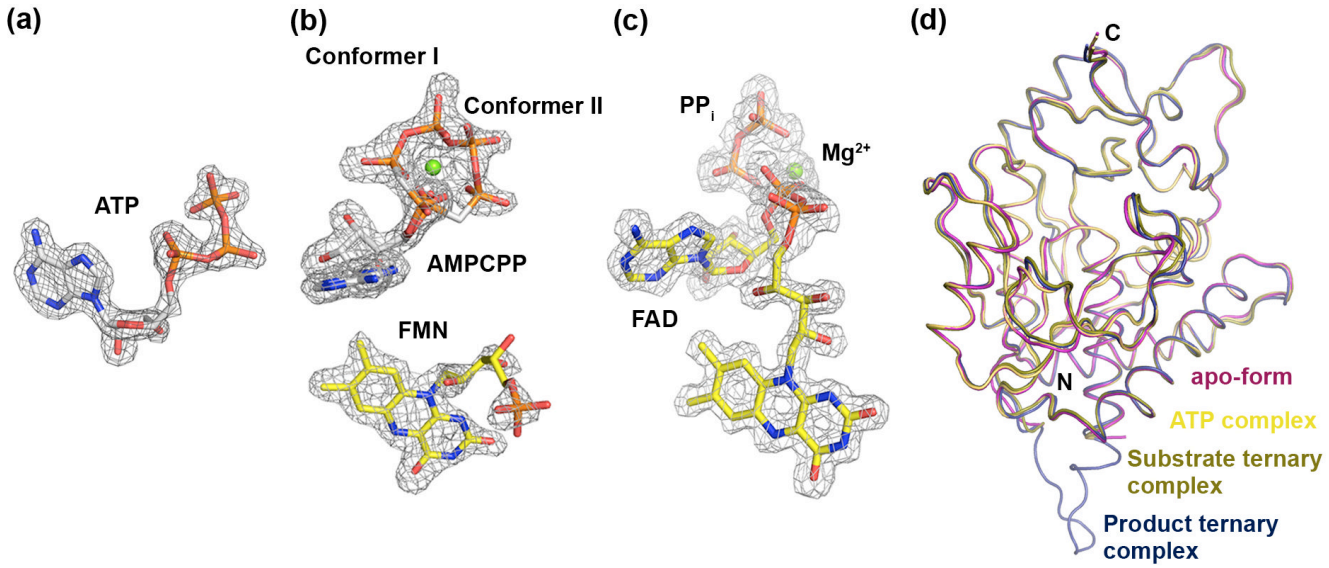

Figure 2. Electron densities of the bound ligands and comparison of *Cg*FMNAT structures

Simulated-annealing F_o-F_c omit maps of (**a**) ATP in the binary complex; (**b**) AMPCPP and FMN in the substrate ternary complex, and (**c**) FAD and PP_i in the product ternary complex. The maps are contoured at 3.0σ for (a) and (c), and 2.5σ for (b). (**d**) Superposition of apo-form (magenta), ATP complex (tan), substrate ternary complex monomer C (dark yellow), and product ternary complex monomer B (dark blue).

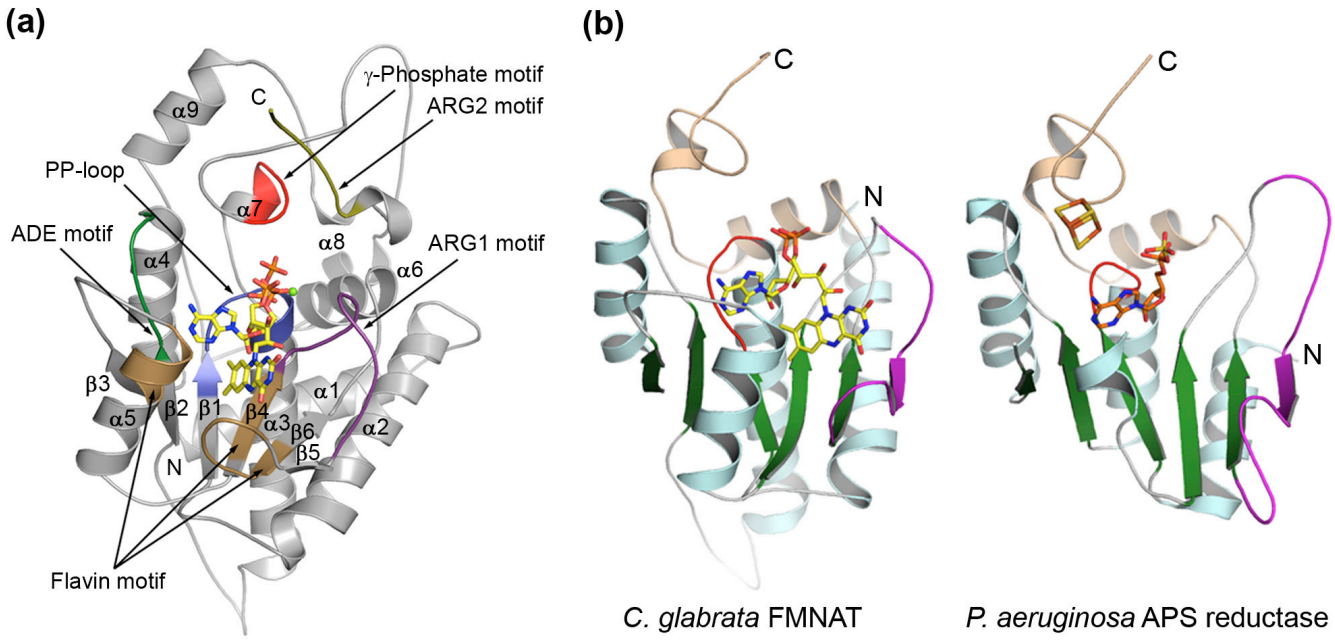

Figure 3. Overall structure of *Cg*FMNAT

(**a**) Ribbon diagram of *Cg*FMNAT structure shown in complex with the products FAD, PP_i, and Mg^{2+}. Secondary structure elements are labeled. Structure motifs involved in substrate binding and catalysis are labeled and highlighted in different colors with *PP-loop* in dark blue, *ADE motif* dark green, *ARG1 motif* magenta, *γ-Phosphate motif* red, and *Flavin Motif* brown. The magnesium ion is shown as a green sphere.

(**b**) Comparison of *Cg*FMNAT with closely related APS reductase. Helix α1 and the last ~70 residues of *Cg*FMNAT are removed for clarity. Bound ligand FAD in *Cg*FMNAT, and APS in APS reductase are shown as sticks colored by atom type with carbon atoms colored yellow and orange, respectively. Equivalent structural motifs are colored similarly. The characteristic PP-loop motifs are colored red. Regions that deviate from the typical Rossmann-fold topology are shown in magenta.

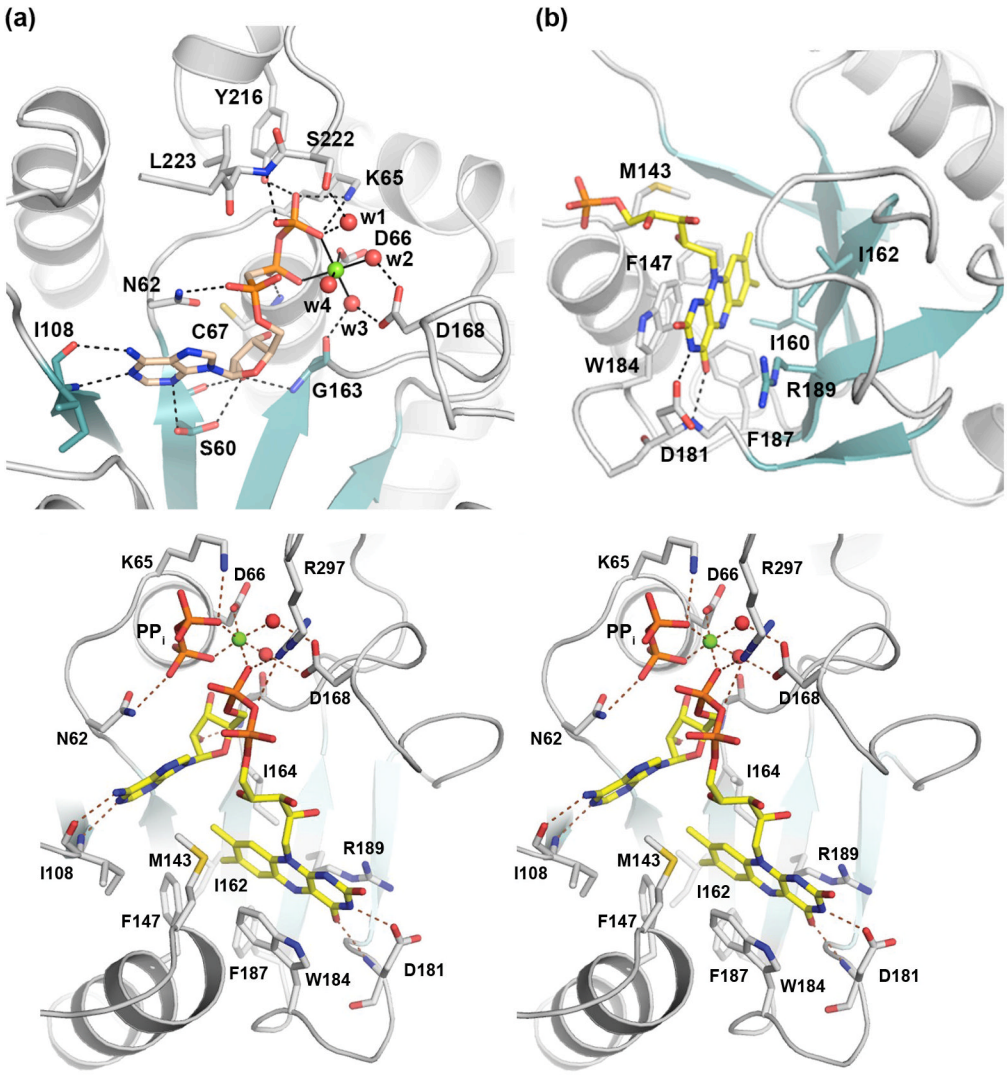

Figure 4. Substrate and product binding in *Cg*FMNAT

(**a**) Details of the Mg^{2+}ATP-binding site. Mg^{2+}AMPCPP in the catalytically relevant conformer I is shown. Protein residues interacting with bound subtrates are shown as sticks. The Mg^{2+} ion is shown as a green sphere and water ligands are shown as red spheres. Hydrogen bonds are shown as dash lines and metal ligands are indicated with solid lines.
(**b**) Details of FMN binding site.
(**c**) Stereo view of FAD and PPi product binding site.

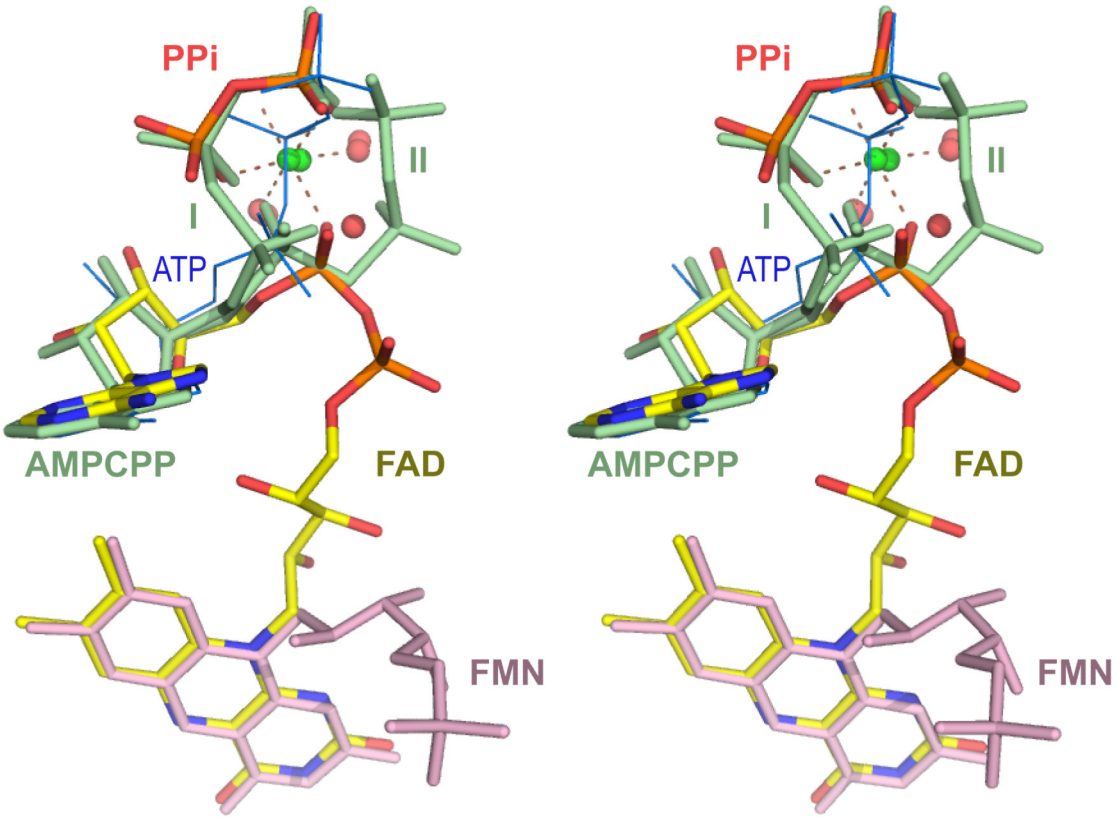

Figure 5. Stereo view of the superposition of bound ATP, Mg^{2+}, FMN and FAD

The dual conformations of AMPCPP (light green) in the substrate ternary complex are marked as I and II. The ATP molecule in the Mg^{2+}-free binary complex structure is shown as blue thin lines. The substrate FMN is colored pink, while the product FAD is colored by atom types with carbon atoms in yellow. The Mg^{2+} ion (green sphere) and corresponding water ligands (red spheres) are also shown.

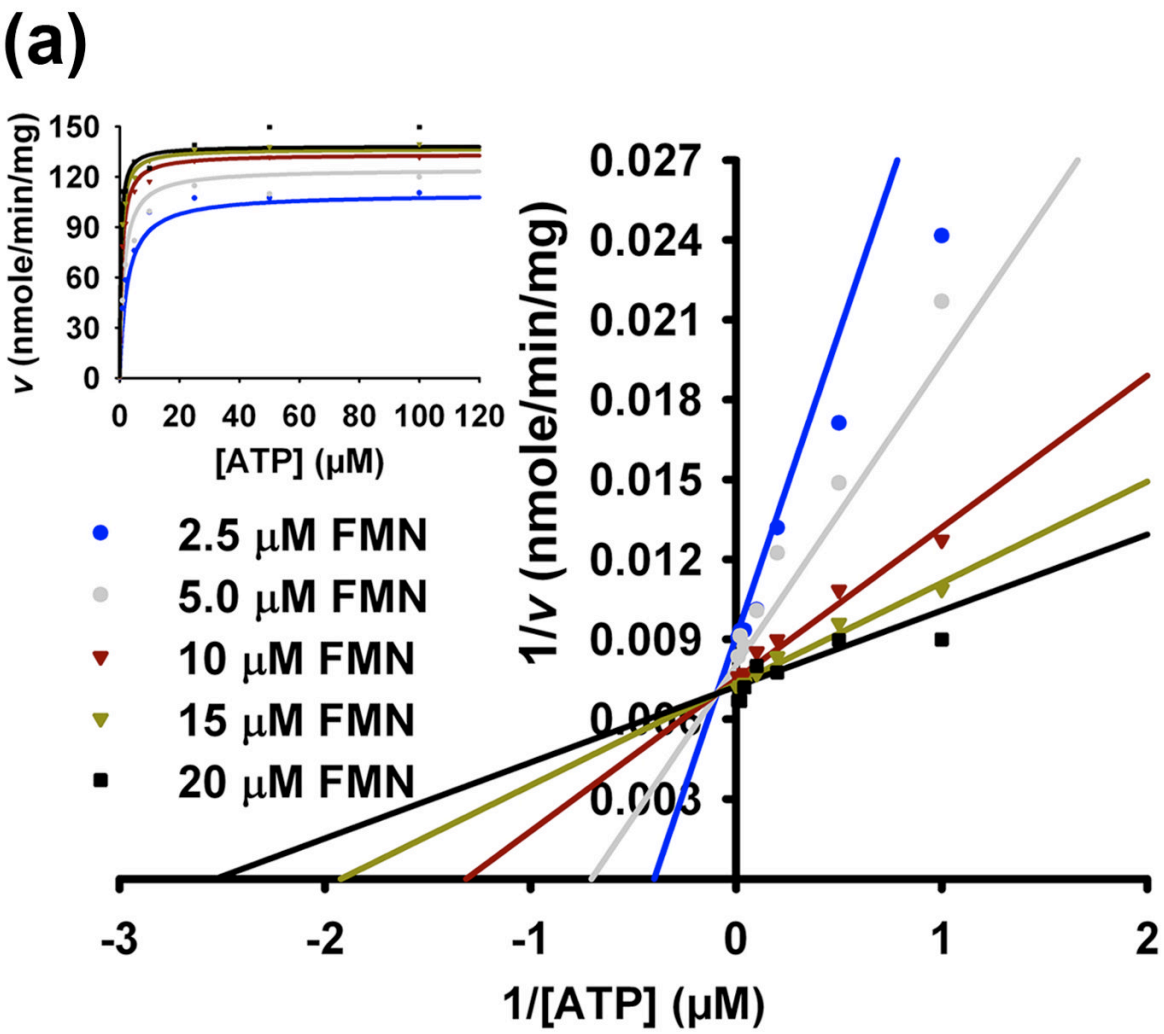

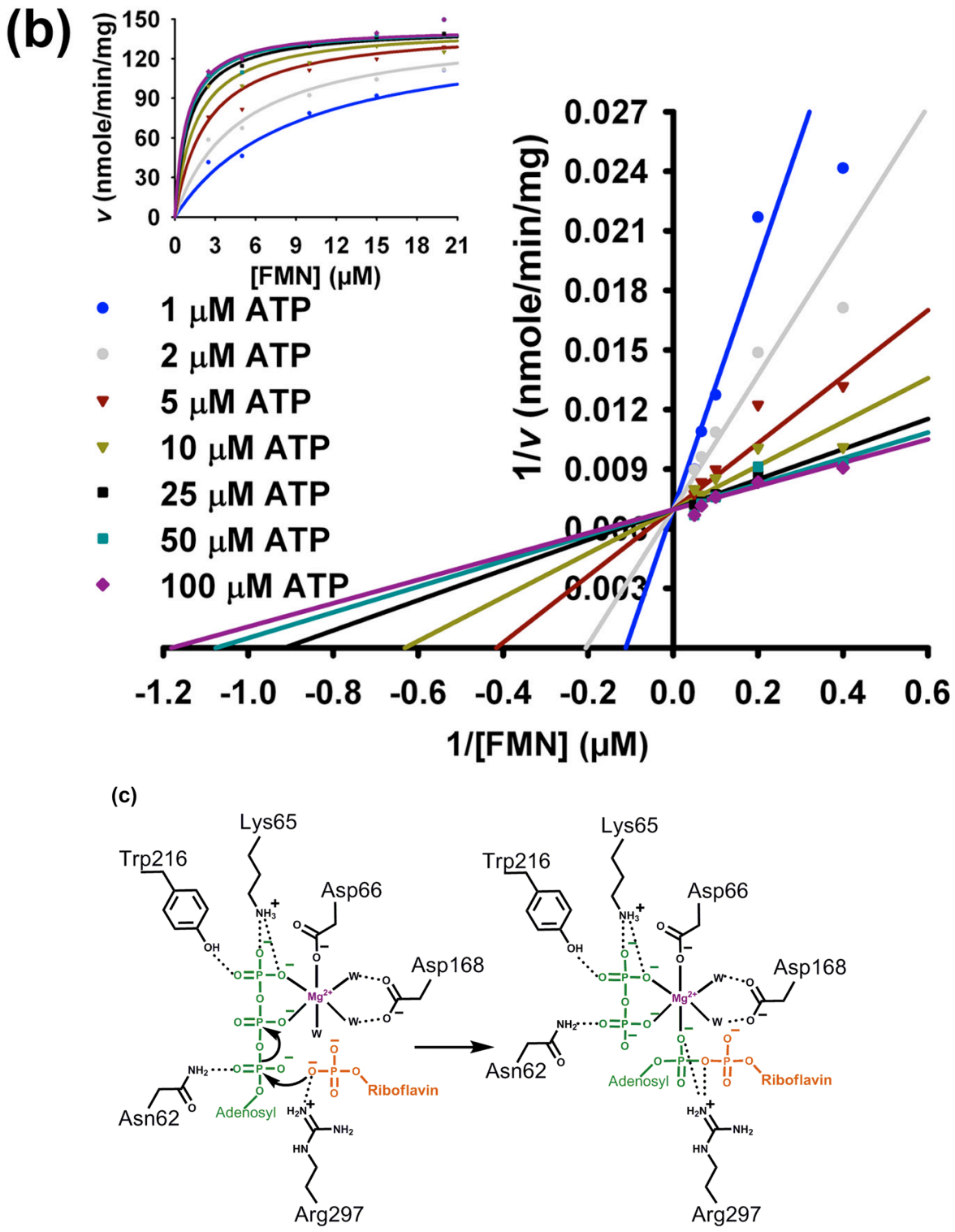

Figure 6. Adenylyl transfer mechanism for *Cg*FMNAT

(**a**) Initial rates represented by Lineweaver-Burk plot of 1/*v* versus 1/[ATP] at fixed FMN concentrations. Insert shows the same data represented by a hypernolic plot (insert) as a function of ATP. (**b**) Initial rates represented by Lineweaver-Burk plot of 1/*v* versus 1/

[FMN] at fixed ATP concentrations. Insert shows the same data represented by a hypernolic plot (insert) as a function of FMN. The rates in (**a**) and (**b**) were globally fitted to the velocity equation for an ordered bi-bi (1) reactant system. (**c**) Proposed catalytic mechanism of *Cg*FMNAT.

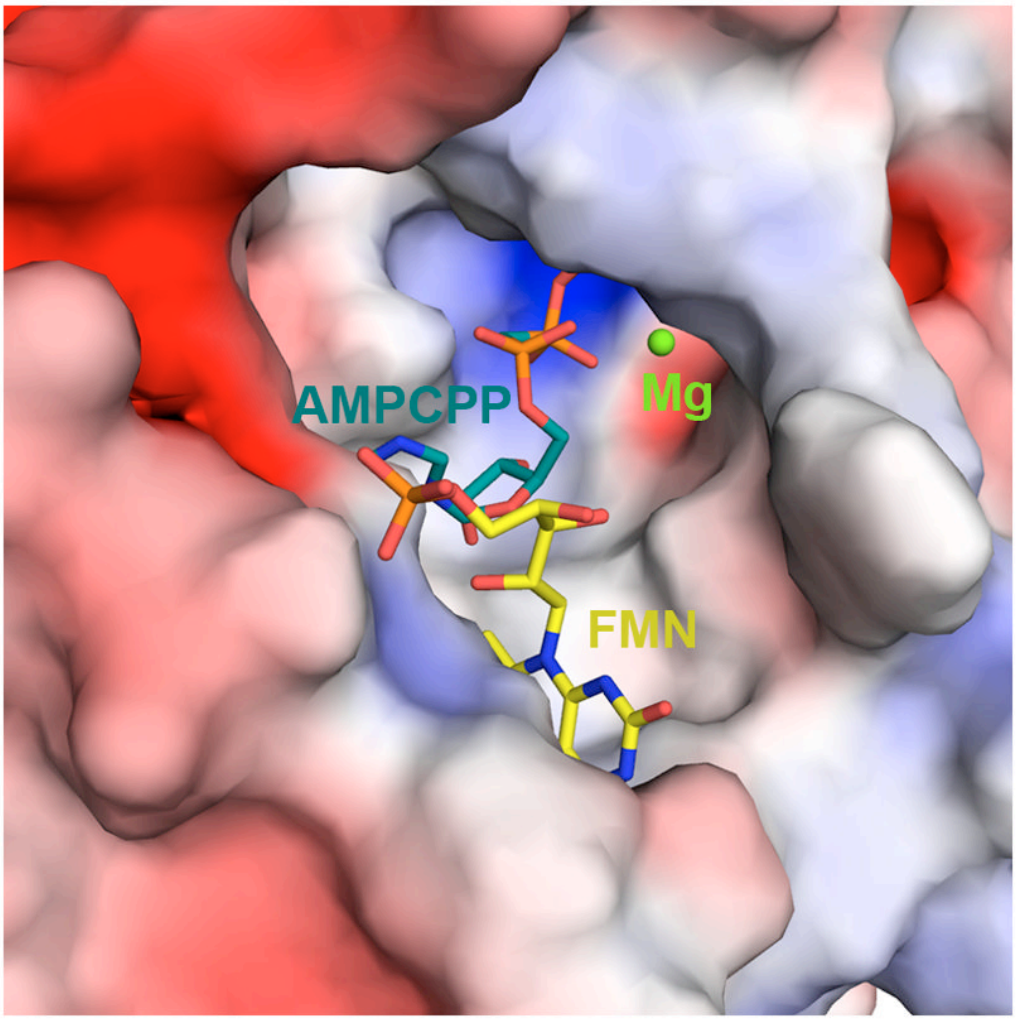

Figure 7. Electrostatic surface potential representation of *Cg*FMNAT substrate binding pocket
The electrostatic potential is color ramped from −5 kT/e (red) to +5 kT/e (blue). FMN and AMPCPP are represented by sticks and Mg^{2+} ion is shown as a green sphere.

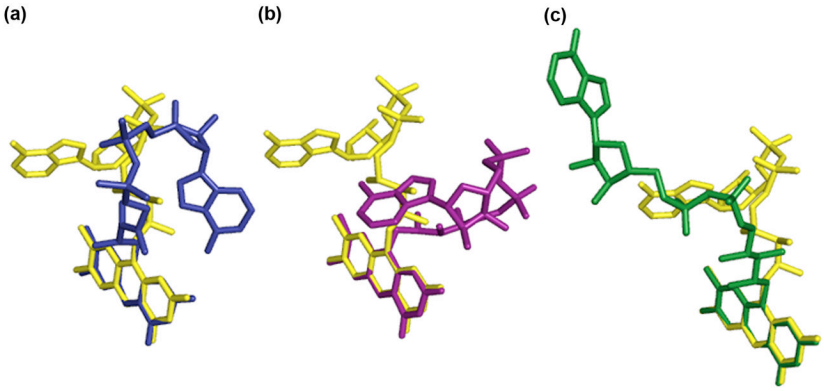

Figure 8. Comparison of protein bound FAD conformations

Representative protein bound FAD molecules were superimposed over the isoalloxazine rings. FAD bound to *Cg*FMNAT (yellow) is compared to FAD from (**a**) flavodoxin reductase (blue) (PDB code 1fdr);[48] (**b**) DNA photolyase (magenta) (PDB code 1dnp);[49] and (**c**) glutathione reductase (green) (PDB code 3grs).[50]

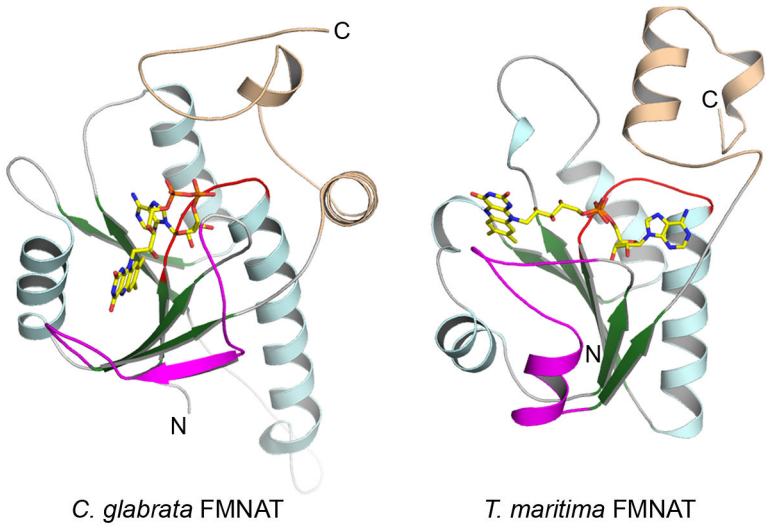

Figure 9. Comparison of eukaryotic and bacterial FMNAT structures

Ribbon diagrams of the Rossmann-like fold core of the *Cg*FMNAT-FAD complex (*left*) and the FMNAT domain of *Tm*FADS (*right*) are shown in roughly the same orientation. An FAD molecule is modeled in the *Tm*FMNAT active site based on the *Tm*FADS-AMP complex structure (PDB identifier 1t6y)[34] and homologous NMNAT-NAD complex structures. Corresponding structural elements are colored identically in the two structures.

Table 1

Data Collection and Refinement Statistics

Protein	**Selenomethionyl apo-*Cg*FMNAT**	**apo-*Cg*FMNAT**	**ATP complex**	**Ternary complex with substrates**	**Ternary complex with products**
Space Group/Monomer per Asymmetric Unit	$P3_221/1$	$P3_221/1$	$P3_221/1$	C2/6	C2/6
Data	SAD	Native	Native	Native	Native
Wavelength (Å)	0.97927	0.97931	1.54178	1.54178	0.97874
Resolution (Å)	50.0−2.18	50.0−1.20	50.0−1.87	50.0−1.95	50.0−1.35
Unit cell dimensions					
a, b, c (Å)	80.31, 80.31, 78.27	80.09, 80.09, 78.09	79.79, 79.79, 77.94	207.83, 81.75, 136.70	206.58, 81.48, 136.60
α, β, γ (°)	90.0, 90.0, 120.0	90.0, 90.0, 120.0	90.0, 90.0, 120.0	90.0, 129.67, 90.0	90.0, 129.79, 90.0
Total no. of reflections	200196	1036966	124769	312183	2800906
No. of unique reflections	15582	90728	24161	123738	380943
% Completeness	99.9 (100.0)[a]	99.9 (99.7)	99.9 (99.6)	96.4 (97.1)	100 (99.8)
R_{sym}[b]	0.091 (0.335)	0.070 (0.442)	0.078 (0.549)	0.088 (0.447)	0.077 (0.551)
I/σ	38.9 (8.5)	48.2 (2.3)	22.0 (2.5)	11.5 (2.1)	35.9 (2.4)
Mosaicity (°)	0.6	0.4	0.7	0.5	0.4
Model Refinement		Anisotropic[e]	Isotropic	Isotropic	Anisotropic
Resolution range (Å)		50.0−1.20	50.0−1.87	35.1−1.95	32.2−1.35
R_{work}[c] (%)		16.2	17.4	17.5	15.3
R_{free}[d] (%)		17.8	22.2	23.6	18.7
No. of protein atoms		2502	2397	14700	14968
No. of ligand atoms		13	44	397	417
No. of water molecules		390	303	1790	1870
Average B-factor (Å^2)					
Protein atoms		17.1	19.3	18.2	17.1
Ligand atoms		21.3	23.5	17.5	15.8
Water molecules		29.3	30.8	28.5	30.4
Rmsd bond length (Å)		0.015	0.015	0.014	0.014

Protein	Selenomethionyl apo-*Cg*FMNAT	apo-*Cg*FMNAT	ATP complex	Ternary complex with substrates	Ternary complex with products
Rmsd bond angle (°)		1.621	1.536	1.458	1.523
Ramachandran Plot					
% favored region		98.6	98.6	98.9	99.1
% allowed region		1.4	1.05	1.1	0.9
% outliers		0.0	0.35	0.0	0.0

[a] Values in parenthesis are for highest-resolution shell.

[b] $R_{sym} = \Sigma_{hkl} [(\Sigma_j (|I_j - \langle I \rangle|)/\Sigma_j I_j]$. $\langle I \rangle$ is the average for all j measurements of reflection hkl.

[c] $R_{work} = \Sigma_{hkl} |F_O - kF_C|/\Sigma_{hkl} |F_O|$, where F_O and F_C are the observed and calculated structure factors, respectively.

[d] R-factor calculated from randomly selected 1.5% (apo-*Cg*FMNAT) or 5% (complexes) reflections that are excluded from refinement for cross-validation.

[e] Six anisotropic thermal factors are used for selected atoms, while isotropic B-factors were used for remaining atoms. Anisotropic thermal parameters were evaluated and assigned using PARVATI[46] and ANISOANL[47].